Journal of Geophysical Research: Solid Earth

RESEARCH ARTICLE
10.1029/2018JB016331

Patterns of Rupture Directivity of Subduction Zone Earthquakes in Northern Chile

Jonas Folesky[1], **Jörn Kummerow**[1], **and Serge A. Shapiro**[1]

[1]Department of Geophysics, Freie Universität Berlin, Berlin, Germany

Key Points:
- A comprehensive study on rupture directivity of seismicity at the rupture region of the 2014 M_W 8.1 Iquique earthquake is conducted
- Directivity is computed for 293 events applying an empirical Green's function approach
- The results display a strongly pronounced preference of rupture directivity toward east (downdip)

Supporting Information:
- Supporting Information S1
- Table S1

Correspondence to:
J. Folesky,
jonas.folesky@geophysik.fu-berlin.de

Citation:
Folesky, J., Kummerow, J., & Shapiro, S. A. (2018). Patterns of rupture directivity of subduction zone earthquakes in northern Chile. *Journal of Geophysical Research: Solid Earth*, *123*, 10,785–10,796. https://doi.org/10.1029/2018JB016331

Received 4 JUL 2018
Accepted 21 NOV 2018
Accepted article online 10 DEC 2018
Published online 15 DEC 2018

Abstract We perform a systematic directivity analysis of local seismic events west off the coast of northern Chile. An empirical Green's function technique is applied to a selection of events from a time period from 2008 to 2016 in the vicinity of the rupture area of the M_W 8.1 Iquique megathrust earthquake in 2014. We compute rupture directivity for 293 events of magnitudes between M_L 2.6 and M_L 5.3. We find a strong preference of rupture orientations subparallel to the convergence vector of the Nazca plate relative to the South-American plate. The preferred rupture direction is downdip. We speculate that the reason for the dominating rupture direction could be a lateral limitation of available rupture directions by the repeating earthquake-like nature of the observed events combined with a material contrast at the subduction interface which, according to the bimaterial effect, favors the downdip rupture direction.

Plain Language Summary We perform a systematic analysis of the direction of the rupture process of earthquakes in northern Chile. To assess the direction of the earthquake ruptures, we use a technique called empirical Green's function analysis. Here a pair of collocated, highly similar earthquakes is used to approximate and then remove the influence of the travel path of the earthquake waves between source and station. Thus, only the signature of the rupture process of the larger event remains, where we can identify the direction of rupture. We analyze events in a time period from 2008 to 2016 in the vicinity of the rupture area of the large M_W8.1 Iquique earthquake in 2014 in northern Chile. We compute rupture directivity for events of magnitudes in the range of M_L2.6 to M_L5.3. We find a striking uniformity of rupture directions which are oriented subparallel to the direction of the plate movement between the Nazca plate and the South-American plate. The preferred rupture direction is directed toward east. We speculate that the reason for the dominating rupture direction could be a limitation of available rupture directions by the special nature of the here analyzed events combined with a material contrast between the two plates.

1. Introduction

It is widely accepted that directivity of seismic events persists at multiple scales (Boatwright, 2007) and thus should be considered when detailed source characteristics are derived from spectral properties (e.g., Kaneko & Shearer, 2014, 2015).

Large earthquakes seem to show preferably unilateral rupture behavior (McGuire et al., 2002), whereas rupture properties of smaller earthquakes are much less frequently analyzed. Rupture propagation imaging for small and medium events ($2 \lesssim M \lesssim 5$) is more difficult to realize due to sparse seismic networks, that is, limited azimuthal coverage or limited resolution relative to the source dimensions. Some studies for medium-sized and small events exist, for example, Boatwright (2007) or Kane et al. (2013). Older studies usually dealt with rupture properties of single earthquakes (Jost et al., 1998; Li et al., 1995), and only recently, larger sets of events were examined for complexities or directivity (Abercrombie et al., 2017; Calderoni et al., 2015; Kane et al., 2013; Lengliné & Got, 2011; Ross & Ben-Zion, 2016). Recent studies also analyzed microseismic events (Dreger et al., 2007; Folesky et al., 2015, 2016; Taira et al., 2015) in an effort to connect with the scales from physical rupture modeling in the laboratory and numerical modeling (e.g., Kaneko & Shearer, 2014, 2015; Lapusta et al., 2000).

A second interesting issue is the conditions under which a preferred directivity may occur. It is current understanding that rupture initiation, propagation, and termination are complex phenomena which are affected by multiple properties such as the material contrast of the juxtaposed rock types at the two sides of a fault (Ben-Zion, 2001; Weertman, 1980). Also, among other aspects, stress state (e.g., Ampuero & Ben-Zion, 2008)

and perturbations of the stress field, for example, by pore pressure changes due to fluid injection, were proposed to affect rupture directivity (Folesky et al., 2016; Shapiro et al., 2011).

The scope of this study is to contribute to the prevailing debate on what controls the directivity of earthquakes. We investigate rupture directivity of multiple small to medium (M_L 2.6–M_L 5.3) events in the northern Chile subduction zone, which were recorded by the Integrated Plate boundary Observatory Chile. On 1 April 2014, the M_W 8.1 Iquique megathrust earthquake occurred in the southern Peru- northern Chile seismic gap (e.g., Hayes et al., 2014; Schurr et al., 2014). This event was preceded by a large number of foreshocks and followed by numerous aftershocks, as, for example, the M_W 7.6 aftershock 3 April 2014, resulting in a high seismicity rate for this region. Multiple large events ($M_L \geq 5$) from this seismic sequence were found to display strong unilateral directivity (Folesky et al., 2018) including the megathrust and its largest foreshock and aftershock (Folesky et al., 2018; Meng et al., 2015; Schurr et al., 2014). The data set also constitutes a rich basis for the here presented comprehensive study on rupture directivity even for events of significantly smaller magnitude. In this manuscript we describe how we compute waveform similarity-based empirical Green's function (EGF) pairs and then reconstruct the source time functions at all recording stations. Further, the amplitudes of these source time functions are analyzed for azimuthal variations corresponding to the directivity effect of unilateral ruptures. The procedure is tested with a synthetic event catalog in order to ensure the robustness of the approach for the given source-receiver geometry in northern Chile. The resulting catalog is finally analyzed for spatiotemporal dependencies of rupture direction and the existence of a preferred rupture directivity.

2. Data: The IPOC Network and Event Catalog

We focus our work on the region of the 2014 M_W 8.1 Iquique event and its foreshock and aftershock series; the spatial extent of the research area ranges from 19.0° to 21.0°S and 69.5° to 71.5°W. We use the seismic CX-net of the Integrated Plate boundary Observatory Chile (IPOC, 2006, see Figure 1) which covers a large part of the back-azimuth window for events occurring in our research area. One hundred hertz, three-component broadband waveform data were accessed via the European Integrated Data Archive web service of GFZ Potsdam (Bianchi et al., 2015). For origin times, locations, magnitudes, and take-off angles, we use the extensive catalog of Sippl et al. (2018) that comprises more than 100,000 events in the northern Chile subduction zone forearc.

To identify suitable candidate earthquake pairs for our EGF analysis, we proceed as follows: We select 9,071 events from the catalog, which are located in the target area of this study, and we use the waveforms obtained at the favorably situated station PB11 as templates for a search of similar events in the continuous seismic waveform data recorded between 2008 and 2016. We apply a bandpass filter between 1 and 4 Hz and cut a 35-s time window which starts 5 s before the *P* pick and includes both *P* and a significant part of the *S* energy. For each filtered template waveform, we then run a cross-correlation detector and identify a suitable EGF-partner for the template event, if the normalized cross-correlation coefficient (CC) exceeds a value of $CC \geq 0.90$ and if the amplitude ratio is higher than 10 or lower than 0.1, corresponding to a magnitude difference of $\Delta M = 1$ between the template and detected event. The high CC calculated for a time window that includes both *P* and *S* phases is a strict criterion to ensure that the interevent distance is very small (e.g., Menke, 1999) and that the difference in travel paths is negligible. Application of these criteria results in a total of 730 candidate EGF-pairs, where the larger EGF-partners are within a range of M_L 2.6 to M_L 5.3. In the following we call these events EGF-pair if a main event has one associated EGF-event and EGF-family if there is one main event having more than one EGF-partner.

3. Method and Testing

An EGF technique based on spectral deconvolution (Li et al., 1995; Mueller, 1985) is used to reconstruct the relative source time functions (RSTFs) of each event at all available stations. This is combined with a directivity analysis based on a model of theoretical variations of the RSTF amplitudes as a function of azimuth for an unilateral rupture (Savage, 1965):

$$F = \frac{A}{K} = \frac{v_r}{1 - (v_r/c) \cdot cos(\phi - \phi_0) \cdot sin(\theta - \theta_0)}. \quad (1)$$

Here F describes the expected amplitude A at a given station, scaled by an unknown constant K. v_r is the rupture velocity, and c is the phase velocity. ϕ is the station azimuth relative to the hypocenter, and θ is the

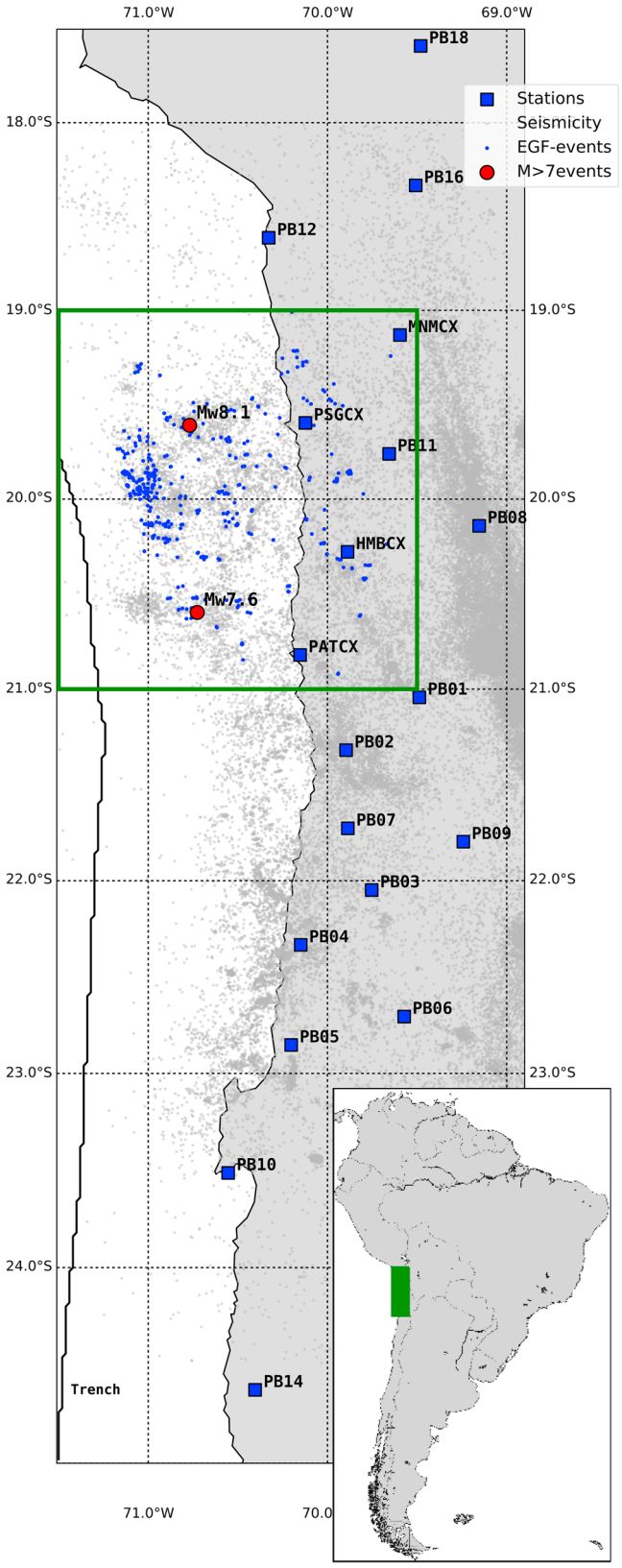

Figure 1. Northern Chile seismicity map view. The locations of Integrated Plate boundary Observatory Chile stations are shown by blue squares. Earthquake locations from the event catalog by Sippl et al. (2018) are marked with gray dots. The study is limited to the area highlighted by the green square. The 730 EGF-pairs from this study are color-coded in blue. The location of the M_W8.1 Iquique event and its biggest aftershock are highlighted red. EGF = empirical Green's function.

ray take-off angle. ϕ_0 is the azimuthal orientation of the rupture direction, and θ_0 describes the dip of the rupture plane.

The procedure is performed using three-component 100-Hz displacement waveforms, where only *P* phases are utilized which are cut out by a fixed 7.5-s time window, starting 1 s before the *P* pick. A 0.8–20-Hz band-pass filter is applied, and the individually reconstructed RSTFs at each component are stacked to obtain an average RSTF for each station. This is repeated station-wise for the entire station network. We fit the amplitude variation model described by equation (1) to the amplitudes obtained from the station-wise reconstructed RSTFs in order to find the rupture direction of the event, that is, we solve for the parameters $\frac{v_r}{c}$ and ϕ_0 (for more details, see Folesky et al., 2016). In the target area, the vast majority of events occur at the plate interface (Sippl et al., 2018) exhibiting similar thrust mechanisms (Cesca et al., 2016) with one fault plane oriented in good agreement with the dipping angle of the subducting slab. We therefore fix the dip of the rupture plane to the subduction angle given in the slab 1.0 model (Hayes et al., 2012). In our case this is implemented by a fixed θ_0, which we use to correct the take-off angles in order to account correctly for the observation point directivity (Kwiatek & Ben-Zion, 2016). This is necessary if stations do not lie on the rupture plane but are vertically offset affecting the recorded waveforms as a consequence of the 3-D character of the directivity effect. With the fixed dip assumption, the number of free parameters in the inversion is reduced to two. For further details and examples on the directivity estimation and the deconvolution approach used, see Folesky et al. (2016) and sources therein.

The accuracy of the procedure is tested for the given data and the event-station configuration in northern Chile by creating a synthetic data set. For this, the observed *P* phases of a randomly selected event out of our EGF-catalog are extracted and then convolved with a scaled Gaussian pulse. The width of the pulse is 0.2 s and the amplitude is set to 10, which corresponds to a magnitude difference of an EGF-pair with $\Delta M = 1$. Depending on the event station back-azimuth, the pulse amplitude and width are varied as described by the model of Savage (1965) for a unilateral propagating rupture. The convolved traces are considered as the waveforms of the main event for the EGF-pair. Then, in a second step, the EGF analysis is performed in order to recompute the initially rupture modeled directions.

Figure 2 exemplarily shows azimuthally sorted source time functions of a simulated EGF-pair. Here we model a horizontal rupture with an azimuthal direction of 60°N and a rupture velocity of $\frac{v_r}{v_p} = 0.5$. Additional noise was added, such that the seismograms of the smaller event partner have a S/N of 20 dB. We estimate a rupture velocity of $\frac{v_r}{v_p} = 0.5$ and a rupture direction toward 67°N, which is close to the modeled values. We repeat this test multiple times for different rupture directions and noise levels. The analysis shows that the statistical error is independent of the modeled rupture direction and increases with noise level. For events with a S/N of 20 dB for the EGF-event, the error is about ±20° and increases to ±40° for a S/N of 10 dB. A detailed description and a summary for the synthetic tests are provided in supporting information S1.

4. Results

Figure 3 shows the RSTFs and the fit of a M_L 3.3 event in the same format as in the previous section. The initial number of 730 suitable pairs is reduced by the data availability, that is, number of stations, their azimuthal distribution, and the number of picks for each event. We require at least six well-reconstructed RSTFs which corresponds to at least six records at six stations including picks. We consider a RSTF at a given station as well reconstructed if it shows a clear pulse-like shape at not less than two of the three components, which have to be of similar shape. Additionally, the stations must cover at least an azimuthal window of 90°. For the event pairs that fulfill these requirements, the directivity is estimated, and a total number of 293 solutions in agreement with the unilateral rupture model is found. These 293 rupture direction estimates still contain several redundancies, because some EGF-families consist of multiple events which results in multiple counts. In Figure 4, waveforms of such an EGF-family are displayed. For the main event (M_L 3.1), six suitable EGF-events (M_L 1.29–M_L 2.10) were identified. For each pair, the directivity analysis was performed separately, and the results are consistent. From 293 separately obtained results, redundancies occur for 134 EGF-pairs which can be grouped into 48 EGF-families, that is, one main event having two or more EGF-events. Note that we do not find an EGF-family with one event being simultaneously the EGF-partner of a bigger main event and having a smaller EGF-partner itself.

We then use the redundancy of estimated rupture directions within an EGF-family to obtain an error estimate on the computed directions for the real data. Due to variations in magnitude and noise, data availability is

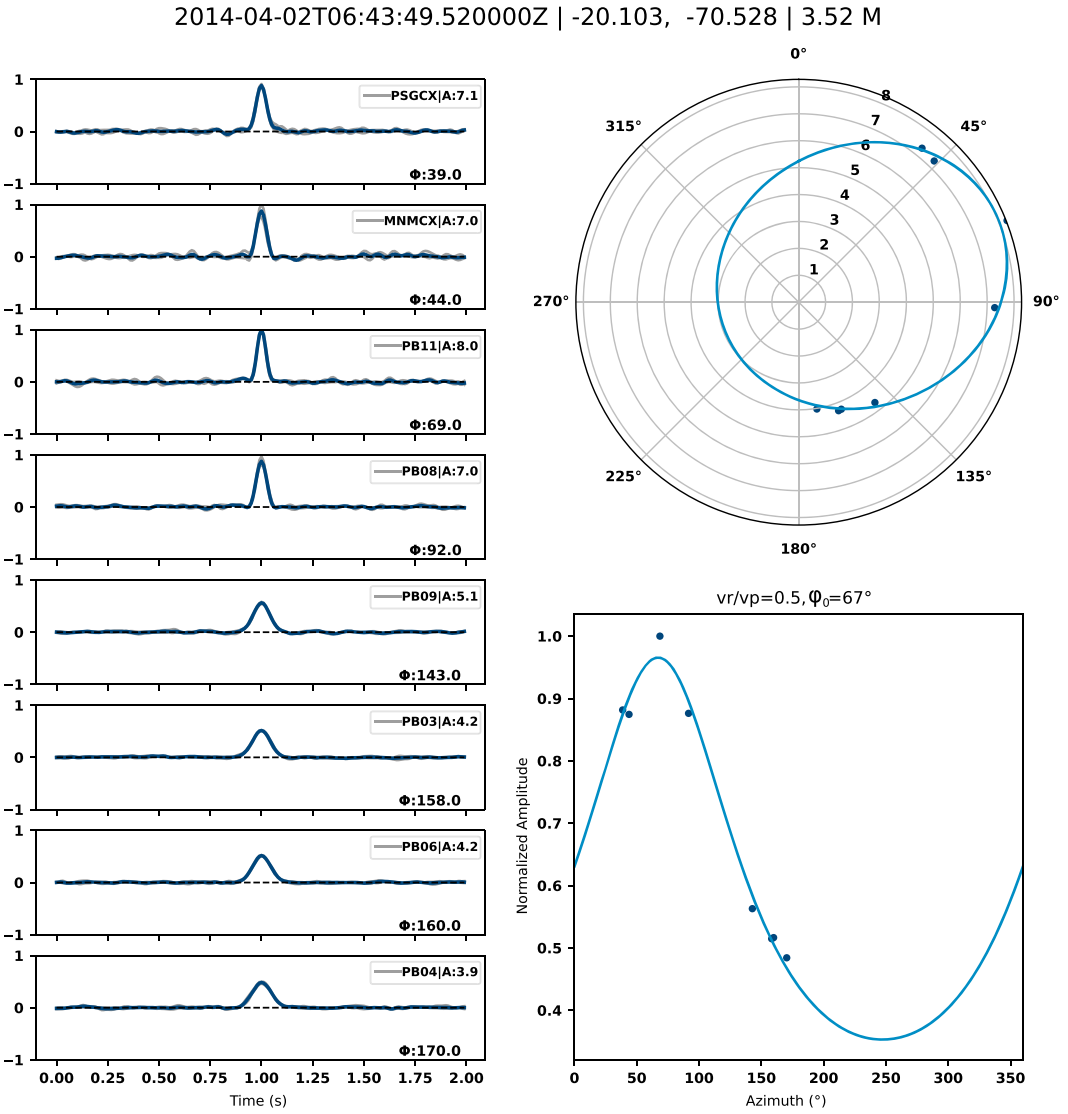

Figure 2. Rupture direction estimation for a synthetic empirical Green's function pair. On the left, azimuthally sorted RSTFs are shown, illustrating the stepwise change of amplitude and width of the pulse due to the modeled characteristics of the directivity effect. The legend states amplitude value of the RSTF, station name, and the station back-azimuth ϕ. On the right, the amplitude measurements of the RSTFs are plotted as black dots at the station back-azimuths. The best fitting unilateral rupture model is shown in rose diagram and sinusoidal form as curve in blue. The true rupture properties were $\frac{v_r}{v_p} = 0.5$ and $\phi_0 = 60°$N. Estimated values are $\frac{v_r}{v_p} = 0.5$ and $\phi_0 = 67°$N. RSTF = relative source time function.

slightly different for each EGF-pair within a family, and the reconstructed RSTFs may show minor differences. We compute an average rupture direction for each EGF-family. Then, we plot the deviation of each single direction estimate to its corresponding family average. The result is shown in Figure 5. We find that the direction estimates within EGF-families are stable and show an average deviation of 14°, while 95% of the computed values are smaller than 35°. We assume that the average error for the non-EGF-family events is similar, and we take the value of $\Delta\phi_0 = 35°$ as a conservative estimate of the fixed statistical error for entire data set. The error estimate is further evaluated by a bootstrap test for all events within the EGF-catalog. This test allows to resolve the robustness of the results for each event. The additional figures show directivity errors, the velocity distribution, and velocity errors. They can be found in supporting information S1.

In a next step, we remove the redundant direction counts from the overall results. In this way we finally obtain 207 independent rupture estimates which are displayed in Figure 6 in map and side views. The figure illustrates the distribution of rupture directions with a strong preference toward east (directions between 30° and 120°N

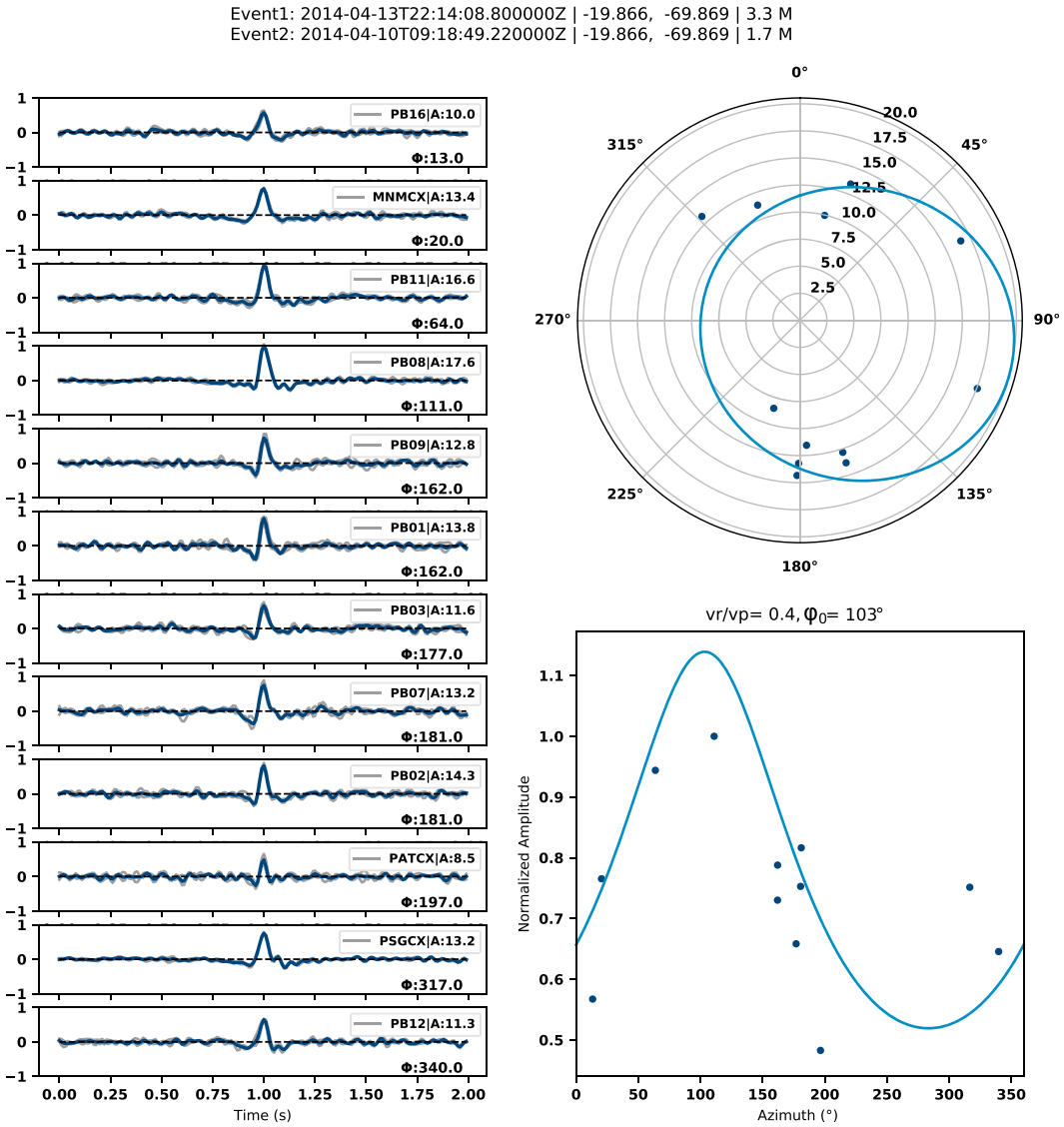

Figure 3. Rupture direction estimate for an empirical Green's function pair consisting of a M_L3.3 and a M_L1.7 event. The relative source time functions on the left are sorted for back-azimuth relative to the event location. The varying pulse amplitudes are measured and plotted to the right as black dots. An unilateral rupture model corresponding to equation (1) is fitted to the data, yielding the rupture direction of ϕ_0 = 103°N and a rupture velocity ratio of $\frac{v_r}{v_p} = 0.4$.

from north). Although generally all rupture directions are found within the distribution, the dominance of the prevailing direction (~80°N) is striking.

The majority of events occur at the plate interface. Some events at 71°W seem to be located at greater depth within the oceanic plate. Note, however, that depth resolution specifically for the offshore events is relatively poor (Sippl et al., 2018). According to their repeating earthquake-like nature (ensured by our waveform similarity-based selection criterion), these events are more likely to have occurred at the plate interface, as the required loading mechanism to produce such events is given there. It is also worth mentioning that we do not find any clear indication of a spatiotemporal dependency within the distribution of rupture directions. The average estimated rupture velocity is $\frac{v_r}{v_p} = 0.49$. For a standard $\frac{v_p}{v_s}$ ratio of 1.73, this translates to an average rupture velocity of about $\frac{v_r}{v_s} \approx 0.85$. Note that the synthetic tests show that the rupture velocity is less reliably recovered than the rupture direction. This is consistent with the observation of Abercrombie et al. (2017) who estimate rupture properties in New Zealand. The result of $\frac{v_r}{v_s} \approx 0.85$ is a typical value for rupture velocity.

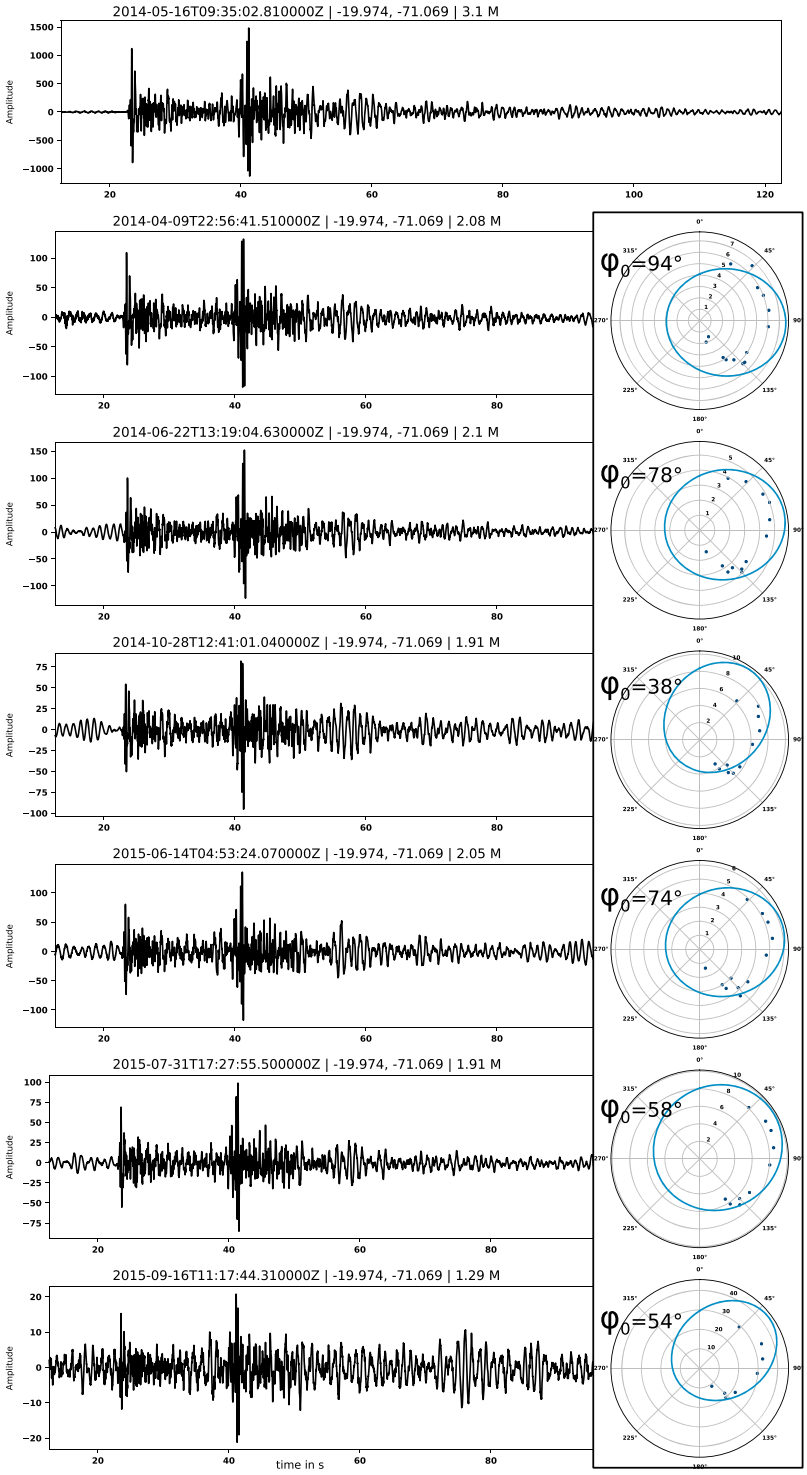

Figure 4. Exemplary EGF-family series. For the main event (M_L 3.1), six EGFs were identified. Displayed are the waveforms obtained at station PB11 for the main event at the top and the EGFs below. The waveforms are sorted by event occurrence date. They show extremely high waveform similarity with the main event. The individually performed rupture directivity results are displayed on the right (cf. Figures 2 and 3). The estimated rupture directions (ϕ_0) are consistent between different EGF-pairs, which is expected, because directivity is a property of the large event partner which is the same for all events. Variations in direction estimates occur mainly due to differing data availability for each event. A statistic on the average deviation of rupture directivity within EGF-families is computed and shown in Figure 5. EGF = empirical Green's function.

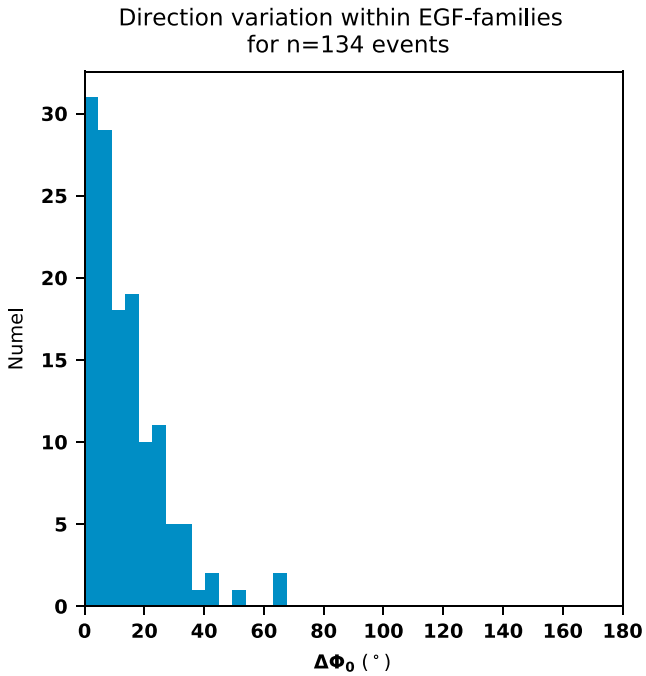

Figure 5. Deviation ($\Delta\phi_0$) between each single EGF-pair rupture direction estimate and its corresponding average EGF-family rupture direction estimate. Low values indicate similar direction estimates within EGF-families. The average deviation is $\Delta\phi_0 = 14°$, while 95% of the computed values are smaller than 35°. EGF = empirical Green's function.

5. Discussion

The observation of a dominant rupture direction at a specific site is not a unique phenomenon. For example, Rubin and Gillard (2000) observed preferred directionality of microearthquakes at the central San Andreas fault based on measurements of the *P* phase pulse width. In contrast, Harris and Day (2005) did not find evidence for a preferred rupture direction based on the rupture processes of Parkfield earthquakes which occurred between 1934 to 2004 and had magnitudes of M > 4. Their results where, however, based on only relatively few events, and their conclusions were subject of an intense debate (Ben-Zion, 2006a, 2006b; Harris & Day, 2005). More recent studies like Lengliné and Got (2011) found evidence for rupture directivity in repeater sequences, and Kane et al. (2013) found preferred oriented directivity for M > 3 events at Parkfield, California.

For the San Andreas fault zone, it therefore seems that a preferred direction exists, although not exclusively. To explain the phenomenon of a preferred rupture direction, the upper mentioned studies refer to the results of Weertman (1980) who found that earthquakes with slip between dissimilar materials produce dynamic changes of normal stress that depend among others on slip direction and material properties of the materials on the two sides of the fault. According to Weertman (1980), a dynamic reduction of normal stress occurs if the rupture direction is in concordance with the slip direction of the more compliant solid. This leads to a preferred direction of rupture propagation, called the bimaterial effect. The solutions are valid for sub-Rayleigh rupture velocities and become reversed for supershear velocities. Also, if slip direction or materials are reversed, a dynamic increase of normal stress on the fault is derived. The nature of ruptures at earthquake faults is of course more complicated than a simple juxtaposition of materials, and the findings of Weertman (1980) were further developed by, for example, Ben-Zion (2001), Shi and Brune (2005), and Ampuero and Ben-Zion (2008), who studied systematically the asymmetry of macroscopic rupture and crack growth. Using numerical simulations, Ampuero and Ben-Zion (2008) found that with strong velocity-weakening friction, pulse-like ruptures show macroscopic asymmetry manifested by significantly larger propagation distance in the preferred direction, corresponding to the bimaterial effect. Additionally, Shi and Brune (2005) found that the effect does not only occur in strike-slip regimes like the San Andreas fault system but is also observable in thrust regimes. The bimaterial effect has also been observed at other locations, for example, in southern California (Ross & Ben-Zion, 2016) and in Italy (Calderoni et al., 2015).

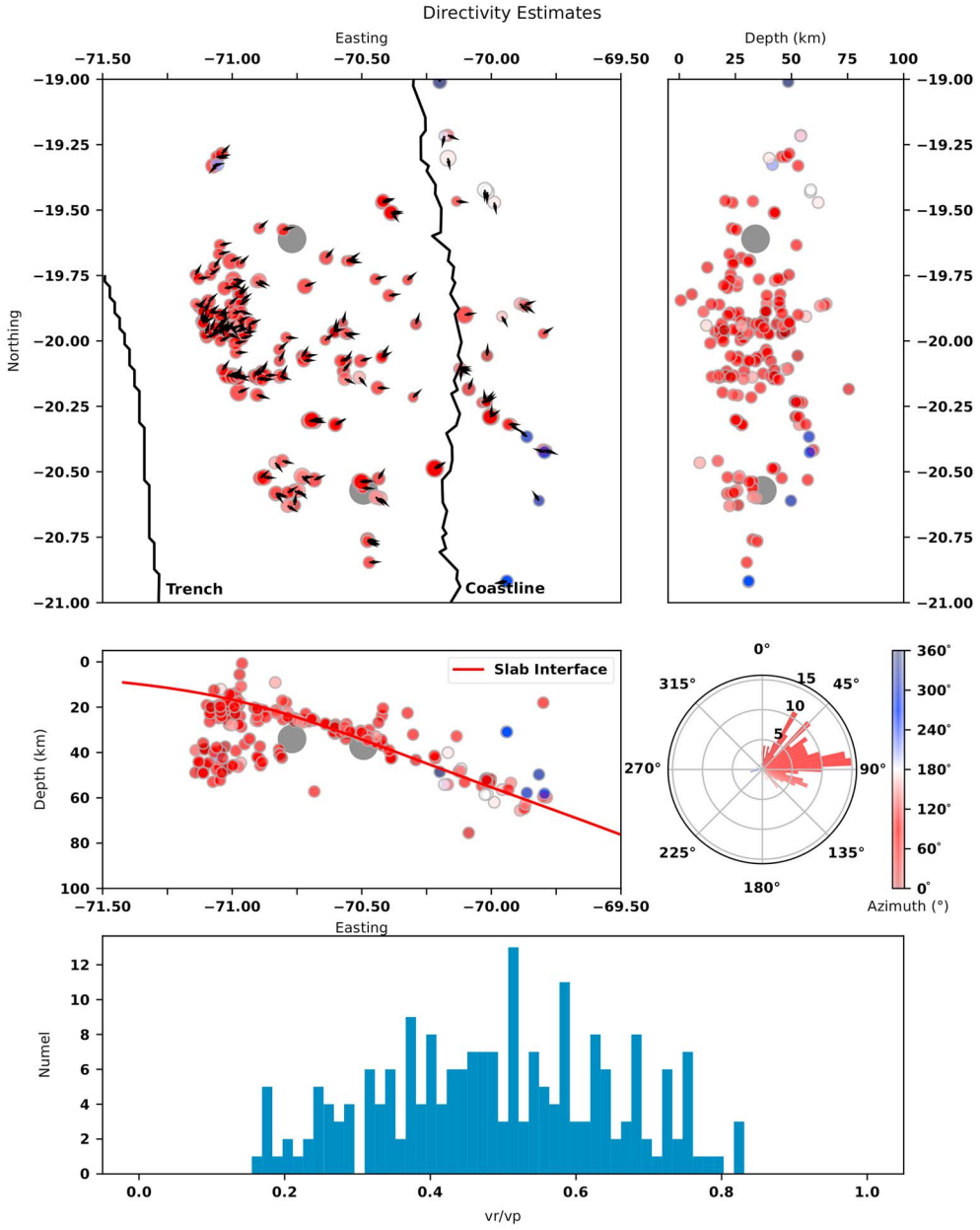

Figure 6. Rupture direction estimates for 207 events from the study area that is highlighted in Figure 1. Top and depth views show the locations of events where we index the rupture direction by a small arrow and a color according to the legend at the bottom right. Reddish colors index eastward directed ruptures; blueish colors show westward directivity. The gray circles are the hypocenters of the mainshock and its largest aftershock, plotted for orientation. The red line is the slab interface after Hayes et al. (2012). The majority of events are oriented eastward in the direction between 30° and 120°N. The statistical error for a single direction estimate is $\Delta\phi_0 = 35°$ (see section 4). The bottom panel shows the rupture velocity ratio $\frac{v_r}{v_p}$. The average velocity ratio is $\frac{v_r}{v_p} = 0.49 \pm 0.16$.

In case of the northern Chilean subduction zone, we find a strong preference of rupture directions toward east, that is, the great majority of events which we analyzed rupture in the downdip direction. According to a wide angle seismic study by Patzwahl et al. (1999), there exists a velocity contrast at the interface between overlying crust and underlying oceanic plate. Their 2-D cross sections show *P* wave velocity distributions down to about 40-km depth. At the plate interface, the velocity of the underlying plate appears to be about 5–10% smaller than the overlying continental crust. According to the bimaterial effect (Weertman, 1980), the preferred rupture direction should consequently be the direction of slip of the more compliant medium, that is, the downdip direction.

While this is a plausible explanation of the observed preferred directivity, it cannot explain the remarkable dominance of rupture directions that we found. As described, we expect events on the slab interface to exhibit the statistical preference to rupture downward due to the bimaterial effect, but heterogeneity in structure and stress field should also play an important role (Ampuero & Ben-Zion, 2008) and widen the range of estimated direction azimuth values. This is indeed observed for larger events at this site. For example, the 2014 8.1 M_W megathrust event and its biggest aftershock (locations in Figure 1) that were located at the plate interface both ruptured to a significant part in the downdip direction (Meng et al., 2015; Schurr et al., 2014). In contrast, the great 6.7 M_W foreshock of the main event was situated in the overlying continental crust (Schurr et al., 2014), that is, it was not affected by the bimaterial effect which was acting at the interface seismicity. According to Meng et al. (2015), this event ruptured northward showing no indication for a downdip component. In addition, Folesky et al. (2018) estimated rupture directivity for 146 $M_L \geq 5$ events in the same research area as this study. They used a *P* wave polarization-based rupture tracking approach and found that generally all rupture directions were present; however, the majority of events ruptured in downdip direction, and a significant amount of events showed a southward-directed rupture component. Generally, their resulting distribution of rupture directivity is more heterogeneous than the one of this work. A possible explanation for this effect is the difference in the databases. In contrast to Folesky et al. (2018), the here presented results are based on a catalog of smaller-sized EGF-pairs. We find many of the features that are reported explicitly for repeating events (cf. Igarashi et al., 2003; Matsuzawa et al., 2004; Nadeau & Johnson, 1998) in our data set as well, as, for example, the very high waveform similarity and thus collocation of the events. Also, we find the great majority of EGF-event locations not within the rupture area of the great M_W 8.1 or M_W 7.6 events but on the up-dip end of their approximate slip area. We observe long lasting sequences of reoccurring EGFs (what we call EGF-families, cf. Figure 4), which can be active over many years as well as clusters of EGF-pairs consisting of only two partners. Following the argumentation of Igarashi et al. (2003), repeating earthquakes nucleate in the area surrounding the slip zone of the large earthquakes. In contrast to the main rupture zone, this area is only weakly coupled and multiple small asperities are distributed on it, that is, strongly coupled asperities are contained in an aseismically creeping zone. Depending on the shape of these postulated asperities, the rupture area for a given repeater is therefore predefined and may only marginally exceed the size of the asperity.

In a detailed study with highly accurate event locations at a creeping section of the San Andeas fault, Rubin et al. (1999) show that many repeating events are situated at elongated streaks which only show an extent in slip direction. We observe a similar pattern in many clusters of EGF events and EGF-families in our data set. Therefore, it appears reasonable to assume that the asperities have an elongated form in direction of the slip direction. If the strength of the asperity is exceeded, a nucleating rupture would consequently have the choice to either rupture up-dip or downdip over the area of the asperity, as the asperity is of less spatial extent in the orthogonal directions. According to the bimaterial effect, the preferred rupture direction should then be the downdip direction, which is what we observe for the given data set. The plate convergence direction in our research area is about 76°N (Angermann et al., 1999), which corresponds well to the preferred directivity (~80°N) found in this study.

Note that we find results for 293 out of 730 suitable event pairs (≈40%). This means that events with unilateral rupture behavior constitute a large part of the total amount of events from the candidate catalog, whereas the remaining events most likely may have different rupture types. Also, the findings are not necessarily representative for nonrepeating earthquake-like events.

6. Conclusions

We have estimated rupture directivity of local seismic events in northern Chile based on an EGF approach. The database for the analysis is a catalog of 730 EGF-pairs that show high waveform similarity, collocation, and a minimum magnitude difference of $\Delta M = 1$ for each event pair. We applied an EGF approach to compute RSTFs for these events, and we fitted a unilateral rupture model to the measured amplitudes of these RSTFs. We found rupture direction estimates for 293 events. By correcting the number of solutions for events with multiple EGF-partners in the catalog, we obtained 207 independent rupture direction estimates. The results show a strong preference (~80°N) of rupture directivity toward east. This corresponds well to the orientation of the convergence vector between Nazca plate and South-American plate (ϕ = 76°N for northern Chile). We propose that the reason for the dominating downdip rupture direction, subparallel to the plate convergence, could be a lateral limitation of available rupture directions for these events. This would correspond to the

concept of repeating earthquakes being confined to an elongated asperity which is situated within an area of aseismic creep. As a result of the bimaterial effect and based on the material contrast at the plate interface and the slip directions of the plates, these laterally confined rupture surfaces should display a preferred downdip rupture direction for such events. Note that such a sharp peak of orientation may only be found because of the a priori selection criteria of the events. Larger events in the region, which are not classified as or even similar to repeaters, show a less strong pronounced but also clear tendency to rupture in downdip direction. We do not find evidence for spatiotemporal dependency of the rupture orientation in our results. Also, no notable influence on the rupture directivity by the main event, for example, due to stress perturbation could be found.

Acknowledgments

J. F. was funded by the German Science foundation, DFG, project SH 55/15-1. We thank the developers and communities of the utilized open source resources (Python 3.5.1 [python.org], IPython 4.2.0, Pérez & Granger, 2007; NumPy, Walt et al., 2011; Matplotlib, Hunter, 2007; ObsPy, Beyreuther et al., 2010; and Lomax et al., 2000), and we thank all institutions involved in operating the IPOC network. We thank C. Sippl for preparation and help with the event catalog. We are also grateful to the editor and two anonymous reviewers for their constructive comments on the manuscript. The EGF-pair catalog from this study is available from the supporting information to this article.

References

Abercrombie, R. E., Poli, P., & Bannister, S. (2017). Earthquake directivity, orientation, and stress drop within the subducting plate at the Hikurangi margin, New Zealand. *Journal of Geophysical Research: Solid Earth*, *122*, 10,176–10,188. https://doi.org/10.1002/2017jb014935

Ampuero, J.-P., & Ben-Zion, Y. (2008). Cracks, pulses and macroscopic asymmetry of dynamic rupture on a bimaterial interface with velocity-weakening friction. *Geophysical Journal International*, *173*(2), 674–692.

Angermann, D., Klotz, J., & Reigber, C. (1999). Space-geodetic estimation of the Nazca-South America Euler vector. *Earth and Planetary Science Letters*, *171*(3), 329–334.

Ben-Zion, Y. (2001). Dynamic ruptures in recent models of earthquake faults. *Journal of the Mechanics and Physics of Solids*, *49*(9), 2209–2244.

Ben-Zion, Y. (2006a). Comment on "Material contrast does not predict earthquake rupture propagation direction" by R.A. Harris and S.M. Day. *Geophysical Research Letters*, *33*, L13310. https://doi.org/10.1029/2005GL025652

Ben-Zion, Y. (2006b). Comment on "The wrinkle-like slip pulse is not important in earthquake dynamic" by D.J. Andrews and R.A. Harris. *Geophysical Research Letters*, *33*, L06310. https://doi.org/10.1029/2005GL025372

Beyreuther, M., Barsch, R., Krischer, L., Megies, T., Behr, Y., & Wassermann, J. (2010). Obspy: A python toolbox for seismology. *Seismological Research Letters*, *81*(3), 530–533.

Bianchi, M., Evans, P. L., Heinloo, A., & Quinteros, J. (2015). Webdc3 web interface, gFZ Data Services. https://doi.org/10.5880/GFZ.2.4/2016.001

Boatwright, J. (2007). The persistence of directivity in small earthquakes. *Bulletin of the Seismological Society of America*, *97*(6), 1850–1861.

Calderoni, G., Rovelli, A., Ben-Zion, Y., & Di Giovambattista, R. (2015). Along-strike rupture directivity of earthquakes of the 2009 L'Aquila, central Italy, seismic sequence. *Geophysical Journal International*, *203*(1), 399–415.

Cesca, S., Grigoli, F., Heimann, S., Dahm, T., Kriegerowski, M., Sobiesiak, M., et al. (2016). The M_w 8.1 2014 Iquique, Chile, seismic sequence: A tale of foreshocks and aftershocks. *Geophysical Journal International*, *204*(3), 1766–1780.

Dreger, D., Nadeau, R. M., & Chung, A. (2007). Repeating earthquake finite source models: Strong asperities revealed on the San Andreas Fault. *Geophysical Research Letters*, *34*, L23302. https://doi.org/10.1029/2007GL031353

Folesky, J., Kummerow, J., Asch, G., Schurr, B., Sippl, C., Tilmann, F., & Shapiro, S. A. (2018). Estimating rupture directions from local earthquake data using the IPOC observatory in Northern Chile. *Seismological Research Letters*, *89*(2A), 495–502. https://doi.org/10.1785/0220170202

Folesky, J., Kummerow, J., & Shapiro, S. A. (2015). Microseismic rupture propagation imaging. *Geophysics*, *80*(6), WC107–WC115.

Folesky, J., Kummerow, J., Shapiro, S. A., Häring, M., & Asanuma, H. (2016). Rupture directivity of fluid-induced microseismic events: Observations from an enhanced geothermal system. *Journal of Geophysical Research: Solid Earth*, *121*, 8034–8047. https://doi.org/10.1002/2016JB013078

Harris, R. A., & Day, S. M. (2005). Material contrast does not predict earthquake rupture propagation direction. *Geophysical Research Letters*, *32*, L23301. https://doi.org/10.1029/2005GL023941

Hayes, G. P., Herman, M. W., Barnhart, W. D., Furlong, K. P., Riquelme, S., Benz, H. M., et al. (2014). Continuing megathrust earthquake potential in Chile after the 2014 iquique earthquake. *Nature*, *512*(7514), 295.

Hayes, G. P., Wald, D. J., & Johnson, R. L. (2012). Slab1. 0: A three-dimensional model of global subduction zone geometries. *Journal of Geophysical Research*, *117*, 1–15. https://doi.org/10.1029/2011JB008524

Hunter, J. D. (2007). Matplotlib: A 2D graphics environment. *Computing In Science & Engineering*, *9*(3), 90–95.

IPOC (2006). IPOC seismic network. Integrated plate boundary observatory Chile - IPOC, GFZ german research centre for geosciences; institut des sciences de lunivers-centre national de la recherche CNRS-INSU, seismic network. https://doi.org/10.14470/PK615318

Igarashi, T., Matsuzawa, T., & Hasegawa, A. (2003). Repeating earthquakes and interplate aseismic slip in the northeastern Japan subduction zone. *Journal of Geophysical Research*, *108*(B5), 2249. https://doi.org/10.1029/2002JB001920

Jost, M. L., Bübelberg, T., Jost, O., & Harjes, H.-P. (1998). Source parameters of injection-induced microearthquakes at 9 km depth at the KTB deep drilling site, Germany. *Bulletin of the Seismological Society of America*, *88*(3), 815–832.

Kane, D. L., Shearer, P. M., Goertz-Allmann, B. P., & Vernon, F. L. (2013). Rupture directivity of small earthquakes at Parkfield. *Journal of Geophysical Research: Solid Earth*, *118*, 212–221. https://doi.org/10.1029/2012JB009675

Kaneko, Y., & Shearer, P. M. (2014). Seismic source spectra and estimated stress drop derived from cohesive-zone models of circular subshear rupture. *Geophysical Journal International*, *197*(2), 1002–1015. https://doi.org/10.1093/gji/ggu030

Kaneko, Y., & Shearer, P. M. (2015). Variability of seismic source spectra, estimated stress drop, and radiated energy, derived from cohesive-zone models of symmetrical and asymmetrical circular and elliptical ruptures. *Journal of Geophysical Research: Solid Earth*, *120*, 1053–1079. https://doi.org/10.1002/2014JB011642

Kwiatek, G., & Ben-Zion, Y. (2016). Theoretical limits on detection and analysis of small earthquakes. *Journal of Geophysical Research: Solid Earth*, *121*, 5898–5916. https://doi.org/10.1002/2016JB012908

Lapusta, N., Rice, J. R., Ben-Zion, Y., & Zheng, G. (2000). Elastodynamic analysis for slow tectonic loading with spontaneous rupture episodes on faults with rate-and state-dependent friction. *Journal of Geophysical Research*, *105*(B10), 23,765–23,789.

Lengliné, O., & Got, J.-L. (2011). Rupture directivity of microearthquake sequences near Parkfield, California. *Geophysical Research Letters*, *38*, L08310. https://doi.org/10.1029/2011GL047303

Li, Y., Doll, C., & Toksöz, M. N. (1995). Source characterization and fault plane determination for M_{blg} = 1.2 to 4.4 earthquakes in the Charlevoix Seismic Zone, Quebec, Canada. *Bulletin of the Seismological Society of America*, *85*(6), 1604–1621.

Lomax, A., Virieux, J., Volant, P., & Berge-Thierry, C. (2000). Probabilistic earthquake location in 3D and layered models. In C. H. Thurber & N. Rabinowitz (Eds.), *Advances in seismic event location* (pp. 101–134). Kluwer, Amsterdam: Springer.

Matsuzawa, T., Uchida, N., Igarashi, T., Okada, T., & Hasegawa, A. (2004). Repeating earthquakes and quasi-static slip on the plate boundary east off northern Honshu, Japan. *Earth, Planets and Space*, *56*(8), 803–811.
McGuire, J. J., Zhao, L., & Jordan, T. H. (2002). Predominance of unilateral rupture for a global catalog of large earthquakes. *Bulletin of the Seismological Society of America*, *92*(8), 3309–3317.
Meng, L., Huang, H., Bürgmann, R., Ampuero, J. P., & Strader, A. (2015). Dual megathrust slip behaviors of the 2014 Iquique earthquake sequence. *Earth and Planetary Science Letters*, *411*, 177–187.
Menke, W. (1999). Using waveform similarity to constrain earthquake locations. *Bulletin of the Seismological Society of America*, *89*(4), 1143–1146.
Mueller, C. S. (1985). Source pulse enhancementt by deconvolution of an empirical Green's function. *Geophysical Research Letters*, *12*, 33–36.
Nadeau, R. M., & Johnson, L. R. (1998). Seismological studies at Parkfield VI: Moment release rates and estimates of source parameters for small repeating earthquakes. *Bulletin of the Seismological Society of America*, *88*(3), 790–814.
Patzwahl, R., Mechie, J., Schulze, A., & Giese, P. (1999). Two-dimensional velocity models of the Nazca plate subduction zone between 19.5° S and 25° S from wide-angle seismic measurements during the CINCA95 Project. *Journal of Geophysical Research*, *104*(B4), 7293–7317.
Pérez, F., & Granger, B. E. (2007). Ipython: A system for interactive scientific computing. *Computing in Science & Engineering*, *9*(3), 21–29.
Ross, Z. E., & Ben-Zion, Y. (2016). Toward reliable automated estimates of earthquake source properties from body wave spectra. *Journal of Geophysical Research: Solid Earth*, *121*, 4390–4407. https://doi.org/10.1002/2016JB013003
Rubin, A. M., & Gillard, D. (2000). Aftershock asymmetry/rupture directivity among central San Andreas Fault microearthquakes. *Journal of Geophysical Research*, *105*(B8), 19,095–19,109.
Rubin, A. M., Gillard, D., & Got, J.-L. (1999). Streaks of microearthquakes along creeping faults. *Nature*, *400*(6745), 635.
Savage, J. C. (1965). The effect of rupture velocity upon seismic first motions. *Bulletin of the Seismological Society of America*, *55*, 263–275.
Schurr, B., Asch, G., Hainzl, S., Bedford, J., Hoechner, A., Palo, M., et al. (2014). Gradual unlocking of plate boundary controlled initiation of the 2014 Iquique earthquake. *Nature*, *512*(7514), 299.
Shapiro, S. A., Krüger, O. S., Dinske, C., & Langenbruch, C. (2011). Magnitudes of induced earthquakes and geometric scales of fluid-stimulated rock volumes. *Geophysics*, *76*(6), WC55–WC63.
Shi, B., & Brune, J. N. (2005). Characteristics of near-fault ground motions by dynamic thrust faulting: Two-dimensional lattice particle approaches. *Bulletin of the Seismological Society of America*, *95*(6), 2525–2533.
Sippl, C., Schurr, B., Asch, G., & Kummerow, J. (2018). Seismicity structure of the Northern Chile forearc from >100,000 double-difference relocated hypocenters. *Journal of Geophysical Research: Solid Earth*, *123*, 4063–4087. https://doi.org/10.1002/2017JB015384
Taira, T., Dreger, D. S., & Nadeau, R. M. (2015). Rupture process for micro-earthquakes inferred from borehole seismic recordings. *International Journal of Earth Sciences*, *104*(6), 1499–1510. https://doi.org/10.1007/s00531-015-1217-8
Walt, S. v. d., Colbert, S. C., & Varoquaux, G. (2011). The NumPY array: A structure for efficient numerical computation. *Computing in Science & Engineering*, *13*(2), 22–30.
Weertman, J. (1980). Unstable slippage across a fault that separates elastic media of different elastic constants. *Journal of Geophysical Research*, *85*(B3), 1455–1461.